

# A Generalized Model for Intersensor NDVI Calibration and Its Comparison With Regression Approaches

Xingwang Fan and Yuanbo Liu

**Abstract**—Satellite remote sensing has accumulated decades of normalized difference vegetation index (NDVI) data. For long-term environmental studies, multisensor NDVI discrepancies should be initially corrected via intersensor NDVI calibration. This paper proposes a generalized model and its simplified form for the calibration by incorporating sensor-, atmosphere-, and observational geometry-related parameters into an analytical function. The models are first validated using the tandem Landsat-5 Thematic Mapper and Earth Observing One (EO-1) Advanced Land Imager (ALI) NDVIs and then used to evaluate current intercalibration methods. The results show that surface reflectance is the most critical factor for linear intercalibrations followed by water vapor. While other atmospheric parameters as well as solar zenith angle have minor effects on linear intercalibrations. The strong nonlinear relationships between the spectral band adjustment factors and NDVI may explain why quadratic functions are used for NDVI intercalibration. Although quadratic intercalibrations are generally more accurate than linear intercalibrations, they may still perform poorly when water vapor exhibits significant spatial variations. In addition, the uncertainties associated with current NDVI intercalibrations are discussed based on the proposed models. This paper furthers the understanding of multisensor NDVI intercalibration and provides insight into intercalibration of other remote sensing indices.

**Index Terms**—Atmosphere, multisensor, normalized difference vegetation index (NDVI) intercalibration, sensor difference, uncertainty.

## I. INTRODUCTION

SATELLITE remote sensing offers favorable opportunities for monitoring long-term environmental changes [1], [2]. Over the past decades, satellite sensors in the solar-reflective spectral domain have acquired massive amounts of data that greatly improve the study of vegetation dynamics [3], [4]. However, differences in two-phase remotely sensed data may not correspond to surface changes due in part to sensor differences [5], [6]. Generally, sensor differences may result from sensor replacement, leading to abrupt changes in relative

spectral response (RSR). For instance, RSRs differ among the analogous bands of Landsat-5 Thematic Mapper (TM), Landsat-7 Enhanced TM plus, and Earth Observing One (EO-1) Advanced Land Imager (ALI) [7]. The RSR effects have been described in [8] as a spectral band difference effect and corrected in [6] using spectral band adjustment factor (SBAF).

Among a variety of vegetation indices, normalized difference vegetation index (NDVI) has been widely used for remote sensing of vegetation [9]. The index is reportedly influenced by various factors, including atmospheric condition [10], surface anisotropy [11], and sensor characteristics [12]–[14]. These influences can be more complicated when multisensor NDVI data are compared for change detection studies. Therefore, NDVI intercalibration is highly needed to generate spatially compatible and temporally consistent NDVI data sets [15]. Currently, most intercalibrations are based on statistical regressions, except for [16], in which a physically based technique was developed from vegetation isoline theory. The technique was applied to a wide range of NDVI values [16]. Since then, several studies have introduced intermediate parameters for NDVI intercalibrations [17]–[19], potentially providing physical insight into empirically based NDVI intercalibrations.

Linear regression has been widely used in a wealth of intercalibration studies [15], [20]. To obtain regression coefficients, data can be acquired from remotely sensed observations (type I), hyperspectral data convolutions (type II), and radiative transfer (RT) calculations (type III). For type I, comparison between coregistered NDVI data yields an intercalibration equation that is generally applicable over a localized area [21]–[25]. This method has been widely used for intercalibration of both top-of-atmosphere (TOA) NDVIs and atmospherically corrected NDVIs [26], [27]. For type II, hyperspectral data are obtained from either *in situ* spectral measurements [15] or satellite hyperspectral observations (e.g., EO-1 Hyperion) [28]. These data are initially convolved with dual-sensor RSRs. Then, the convolved data are regressed for intercalibration equations. Due to the limited availability of hyperspectral data, these studies are generally restricted to local scales and even to unique land cover types [29]. For type III, RT codes are executed for TOA spectral band reflectances (and thus TOA NDVIs) over a wide range of surface reflectances, atmospheric conditions, and observational geometries [20]. The surface reflectance data can be

Manuscript received January 28, 2016; revised April 18, 2016 and November 23, 2016; accepted December 1, 2016. Date of publication December 23, 2016; date of current version February 23, 2017. This work was supported in part by the National Natural Science Foundation of China under Grant 41171272 and in part by the Talent Introduction Project of the Nanjing Institute of Limnology and Geography, Chinese Academy of Sciences under Grant NIGLAS2015QD08.

The authors are with the Nanjing Institute of Geography and Limnology, Chinese Academy of Sciences, Nanjing 210008, China (e-mail: xwfan@niglas.ac.cn; ybliu@niglas.ac.cn).

Color versions of one or more of the figures in this paper are available online at <http://ieeexplore.ieee.org>.

Digital Object Identifier 10.1109/TGRS.2016.2635802

simulated using canopy models and/or acquired from spectral libraries [30].

In addition to linear regression, the empirically based intercalibration also includes quadratic regression. The quadratic regression has been widely used to address the nonlinearities associated with NDVI intercalibration [31]. Using the type III data, Trishchenko *et al.* [32], [33] developed quadratic functions for NDVI intercalibration between National Oceanic and Atmospheric Administration (NOAA) Advanced Very High Resolution Radiometers (AVHRRs) and NOAA-9 AVHRR. Quadratic regression has also been used in [34] for NDVI intercalibration among major fine-resolution sensors and in [30] for NDVI intercalibration among major coarse-resolution sensors. Overall, these studies generally collect multisource surface reflectance data, simulate TOA NDVI data under varying observational geometries and atmospheric conditions, and calculate quadratic functions. The resulting functions are reportedly applicable to spatially and temporally different scenarios.

Generally, both linear and quadratic regressions provide operational solutions to resolve multisensor NDVI inconsistencies. Nevertheless, empirically based methods should be supported with physical background data. For instance, both linear and exponential functions can be used to model the relationship between NDVI and leaf area index [35], [36]. In fact, the principle behind the functions is the variation in fractional vegetation cover [37]. Quadratic regression may perform better than linear regression from a mathematical perspective. However, it remains unclear why linear and quadratic functions are used. Additionally, the conditions for which linear functions are sufficiently accurate still require backup information and supporting evidence. Only with physical background data can the applicability and uncertainty of empirically based methods be evaluated.

The objective of this paper is to evaluate current NDVI intercalibration methods in terms of application condition and possible uncertainty. For this purpose, analytical functions that incorporate SBAFs, atmospheric conditions, and observational geometry parameters are developed for NDVI intercalibration. The functions are validated and used to investigate critical factors that may affect NDVI intercalibration. Subsequently, we clarify the applicable conditions of the linear and quadratic functions for NDVI intercalibration, and investigate the possible causes of the associated uncertainties. The results would deepen our understanding of multisensor NDVI intercalibration. This paper is structured as follows: Section II states the methodology, Section III describes the materials and data processing, Sections IV and V present the major findings and their implications for NDVI intercalibration, and Section VI is the conclusion.

## II. METHODOLOGY DEVELOPMENT

### A. Generalized Function for NDVI Intercalibration

Based on TOA reflectances in the red band ( $R$ ) and the near-infrared (NIR) band ( $N$ ), the NDVI is defined as follows:

$$\text{NDVI} = \frac{\rho_{\text{TOA},N} - \rho_{\text{TOA},R}}{\rho_{\text{TOA},N} + \rho_{\text{TOA},R}}. \quad (1)$$

TABLE I  
SYMBOLS AND DEFINITIONS

Symbol	Definition	Dimension/Units
NDVI	Normalized Difference Vegetation Index	Dimensionless
TOC	Total Ozone Concentration	$\text{cm} \cdot \text{atm}^{-1}$
TPW	Total Precipitable Water vapor content	$\text{g} \cdot \text{cm}^{-2}$
AOT	Aerosol Optical Thickness at 550 nm	Dimensionless
SZA	Solar Zenith Angle	Degrees
VZA	View Zenith Angle	Degrees
SBAF	Spectral Band Adjustment Factor $f$	Dimensionless
R/NIR	Red/Near-infrared band, denoted by $R/N$	Dimensionless
RSR	Relative Spectral Response	%
$\rho_{\text{TOA}}$	TOA reflectance	%
$\rho_a$	Path radiance in reflectance units	%
$\rho$	Surface reflectance	%
$T_g$	Atmospheric absorption transmittance	Dimensionless
$T_s$	Atmospheric scattering transmittance ↓	Dimensionless
$T_v$	Atmospheric scattering transmittance ↑	Dimensionless
$A$	Accuracy index	NDVI units
$P$	Precision index	NDVI units
$U$	Uncertainty index	NDVI units
$n_1, n_2, \varphi$	Intermediate variables of models	Dimensionless

With respect to TOA reflectance, an intersensor relationship has been developed in our previous studies [38], [39]

$$\rho_{\text{TOA},2} = \underbrace{\left( f_{2/1} \times \frac{T_g T_s T_v}{T_g T_s T_v} \right)}_a \times \rho_{\text{TOA},1} + \underbrace{T_g \left( \rho_{a,2} - f_{2/1} \times \rho_{a,1} \times \frac{T_s T_v}{T_s T_v} \right)}_b \quad (2)$$

where  $f$  is SBAF,  $T_g$  is atmospheric absorption transmittance,  $T_s$  and  $T_v$  are two-way atmospheric scattering transmittances, and  $\rho_a$  is path radiance. Functions of these variables are detailed in [38] and shown in the Appendix. Subscripts 1 and 2 denote two sensors, and  $a$  and  $b$  denote the multiplicative and additive components.

Combining (1) and (2) yields the following equation:

$$\begin{aligned} \text{NDVI}_2 &= \frac{(a_N + a_R)\text{NDVI}_1 + (a_N - a_R) + 2(b_N - b_R)/(R_1 + \text{NIR}_1)}{(a_N + a_R) + (a_N - a_R)\text{NDVI}_1 + 2(b_N + b_R t)/(R_1 + \text{NIR}_1)} \end{aligned} \quad (3)$$

where  $a$  and  $b$  denote the multiplicative and additive components in (2).

### B. Simplified Function for NDVI Intercalibration

Under the assumptions that  $b_R \ll 1$  and  $b_N \ll 1$ , (3) is simplified as follows:

$$\text{NDVI}_2 = \frac{n_1 \times \text{NDVI}_1 + n_2}{n_1 + n_2 \times \text{NDVI}_1} \quad (4)$$

where  $n_1 = a_N + a_R$  and  $n_2 = a_N - a_R$  are the analytical functions of SBAFs, atmospheric parameters, and observational geometry parameters. For clarification, the major symbols and definitions are summarized in Table I.

### C. Statistical Monte Carlo Method

The statistical Monte Carlo method is a computational algorithm that relies on random and repeated sampling to obtain approximate results [40]. This method can be used to obtain numerically approximate solutions to problems without analytical solutions, such as NDVI intercalibration. It is used here to randomly sample various parameters [subject sensor NDVI, ozone concentration, water vapor content, aerosol optical thickness (AOT), SBAF, and solar zenith angle (SZA)] within their reasonable ranges. Reference sensor NDVIs can be generated by entering these randomly sampled parameters into (4).

### D. Indices for Evaluating NDVI Intercalibration

The indices include accuracy ( $A$ ), precision ( $P$ ), and uncertainty ( $U$ )

$$A = \frac{\sum_{i=1}^N (\text{NDVI}_2^i - \text{NDVI}_1^i)}{N} \quad (5a)$$

$$P = \sqrt{\frac{\sum_{i=1}^N (\text{NDVI}_2^i - \text{NDVI}_1^i - A)^2}{N - 1}} \quad (5b)$$

$$U = \sqrt{\frac{\sum_{i=1}^N (\text{NDVI}_2^i - \text{NDVI}_1^i)^2}{N}} \quad (5c)$$

where superscripts 1 and 2 denote two sensors, and  $N$  denotes the total number of NDVI samples ( $i \leq N$ ).

The accuracy index  $A$  shows the mean NDVI difference and  $A \neq 0$  indicates the existence of systematic bias. The precision index  $P$  shows the standard deviation of NDVI differences and  $P \rightarrow 0$  indicates good NDVI consistency if systematic bias is removed, while the uncertainty index  $U$  is an overall representation of NDVI differences [41].

## III. STUDY MATERIALS AND DATA PROCESSING

### A. Remotely Sensed Data

The data used for NDVI intercalibration are Landsat-5 TM and EO-1 ALI images. The TM has one red band and one NIR band. The ALI has one red band and two NIR bands (Fig. 1). The red bands are spectrally similar between TM (0.626–0.693  $\mu\text{m}$ ) and ALI (0.633–0.690  $\mu\text{m}$ ). The two NIR bands (NIR1: 0.775–0.805  $\mu\text{m}$ ; NIR2: 0.845–0.890  $\mu\text{m}$ ) onboard the ALI sensor are both spectrally narrower than the TM NIR band (0.776–0.904  $\mu\text{m}$ ).

Hyperion image and MODerate-resolution Imaging Spectroradiometer (MODIS) atmospheric data are used to calculate (3) and (4). Hyperion has 242 spectral bands in the solar-reflective spectral domain, with a spectral resolution of  $\sim 10$  nm. All images (TM, ALI, and Hyperion) were acquired within WRS-2 121/41 on October 31, 2005, covering part of the Poyang Lake basin, China (Fig. 2). For TM, an additional image within WRS-2 121/40 was acquired to fully cover the spatial extent of ALI and Hyperion images. The TM images were collected between UTC 2:32:10–2:33:00, the ALI image was collected between UTC 2:32:17–2:32:29, and the Hyperion image was collected between UTC 2:32:15–2:32:29. The minor time differences

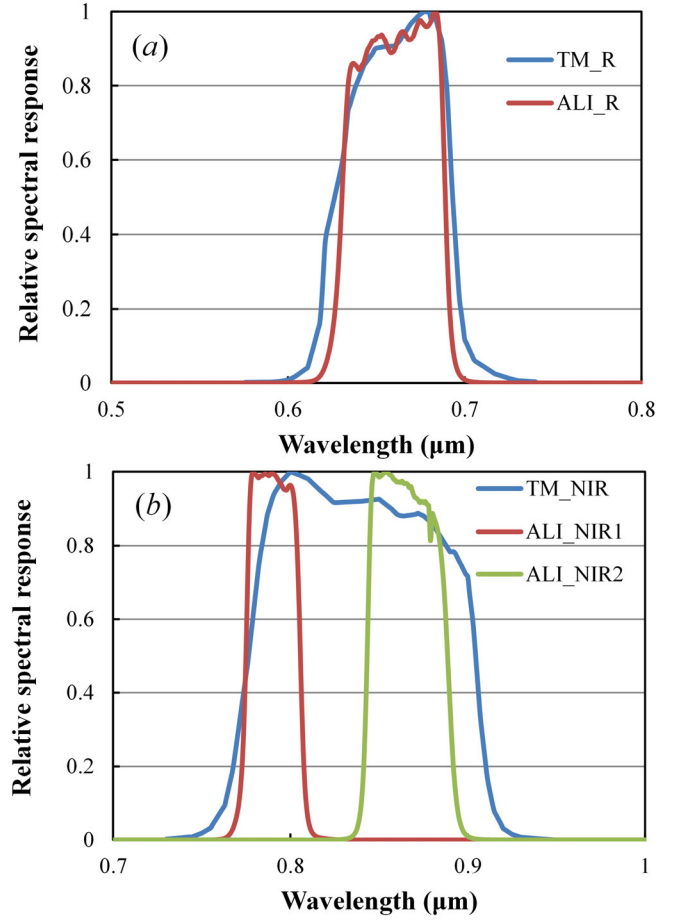


Fig. 1. RSRs of TM and ALI red and NIR bands.

ensured stable atmospheric conditions and an invariant land surface during sensor overpasses. The atmospheric data were collected from the TERRA MODIS Level-2 scientific data sets, including MOD04 AOT (AOT at 550 nm), MOD07 total ozone concentration (TOC), and total precipitable water vapor (TPW). Because the TERRA satellite overpassed  $\sim 20$  min earlier than EO-1 and Landsat-5, the assumption was that the atmosphere remained relatively stable during the overpasses.

### B. Preprocessing of Remotely Sensed Data

The overlapping area of remotely sensed images was retained for intercalibration (Fig. 2). Within the region of interest, Hyperion image was converted to surface reflectances, and TM/ALI images were converted to TOA reflectances. The Hyperion data were initially converted to spectral radiances using the coefficients in [42] and then atmospherically corrected via the fast line-of-sight atmospheric analysis of spectral hypercubes [43]. For atmospheric correction, the atmospheric model was midlatitude winter and the aerosol model was rural. AOTs were retrieved using the 660-nm and 2100-nm bands, and TPWs were retrieved using the 1135-nm band. For TM and ALI, TOA reflectances were calculated using the coefficients in [7].

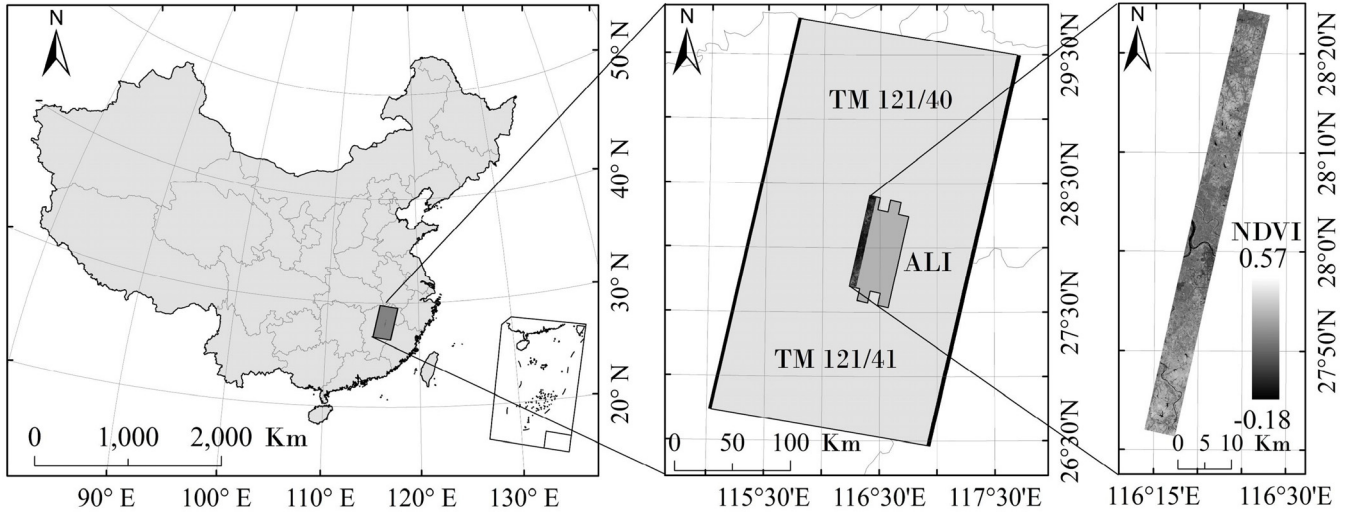


Fig. 2. Geolocation of the study area. Middle frame: relative position of the remotely sensed images. Right frame: TM NDVI in the region of interest.

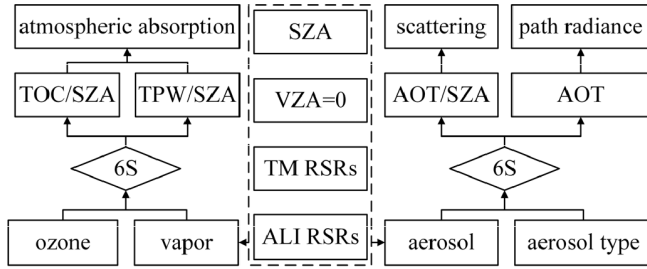


Fig. 3. Flowchart of coefficients determination using the 6S RT codes.

Hyperion surface reflectance data were used to calculate SBAFs, and TM/ALI TOA reflectance data were used to generate NDVIs. To reduce the effects of spatial misregistration, all data were aggregated from  $30 \text{ m} \times 30 \text{ m}$  pixels to  $300 \text{ m} \times 300 \text{ m}$  grids. The aggregated Hyperion data were then spectrally convolved according to TM and ALI RSRs. The SBAFs were calculated as the ratio of the ALI-convolved reflectances to the TM-convolved reflectances in the analogous bands (A1). In addition, TM and ALI NDVIs were calculated using (1) and further used for intercalibration. Notably, two NIR band SBAFs and NDVIs were calculated for ALI. Finally, the center coordinates of the  $300 \text{ m} \times 300 \text{ m}$  grids were used to extract AOT, TOC, and TPW values from the corresponding MODIS scientific data.

### C. Radiative Transfer Calculations

In [38], atmospheric absorption transmittance is an analytical function of TOC and TPW (A2)–(A4), and atmospheric scattering transmittance and path radiance are the analytical functions of AOT (A5) and (A6). The function coefficients are sensor-dependent, and can be determined using the second simulation of the satellite signals in the solar spectrum (6S) RT code [44] (Fig. 3). The code was executed at different TOC ( $0.247\text{--}0.480 \text{ cm} \cdot \text{atm}^{-1}$ ), TPW ( $0.1\text{--}4.1 \text{ g} \cdot \text{cm}^{-2}$ ), AOT ( $0.1\text{--}1.0$ ), and SZ A ( $0\text{--}60^\circ$ ) levels [38]. The spectral

bands were set as TM/ALI red and NIR bands, and the VZA view zenith angle was set as nadir-looking. Aerosol type was set as continental according to the geographical location of our study area. Using the simulated data, function coefficients were determined under the constraint of least squares.

### D. TM and ALI NDVI Intercalibrations

Four methods were employed for NDVI intercalibration, including the generalized model, the simplified model, linear regression, and quadratic regression. For the generalized and simplified NDVI intercalibrations, the right-hand sides of (3) and (4) were calculated using the aforementioned data and compared with the left-hand sides. In (3) and (4),  $\text{NDVI}_1$  referred to TM NDVIs, and  $\text{NDVI}_2$  referred to ALI NDVIs. Accuracy, precision, and uncertainty indices were used to evaluate the intercalibrations. For the linear and quadratic regression-based NDVI intercalibrations, TM NDVI served as the independent variable, and ALI NDVI served as the dependent variable.

### E. Assignments for Monte Carlo Method

Equation (4) is primarily controlled by the TOC, TPW, AOT, SBAF, and SZ A. Because of no reflectance items, it is a better choice for simulations than (3). To investigate the major factor(s) that may affect NDVI intercalibration,  $\text{NDVI}_2$  in (4) was simulated based on different TOC ( $0.25\text{--}0.48 \text{ cm} \cdot \text{atm}^{-1}$ ), TPW ( $0.0\text{--}2.0 \text{ g} \cdot \text{cm}^{-2}$ ), AOT ( $0.0\text{--}1.0$ ), SBAF ( $0.9\text{--}1.1$ ), SZ A ( $0\text{--}60^\circ$ ), and  $\text{NDVI}_1$  ( $0.0\text{--}1.0$ ) levels. The low (high) TPW and AOT values corresponded to dry (wet) and clear (turbid) atmospheric conditions. Both low and high SBAF values denoted large sensor differences. The range of SZ A covered most remotely sensed images suitable for practical applications. Because we primarily focus on the land surface,  $\text{NDVI}_1$  was assigned 10000 random values in the range of  $0.0\text{--}1.0$ . For the simulation of a specific factor, the other factors were assigned median values (Table II).

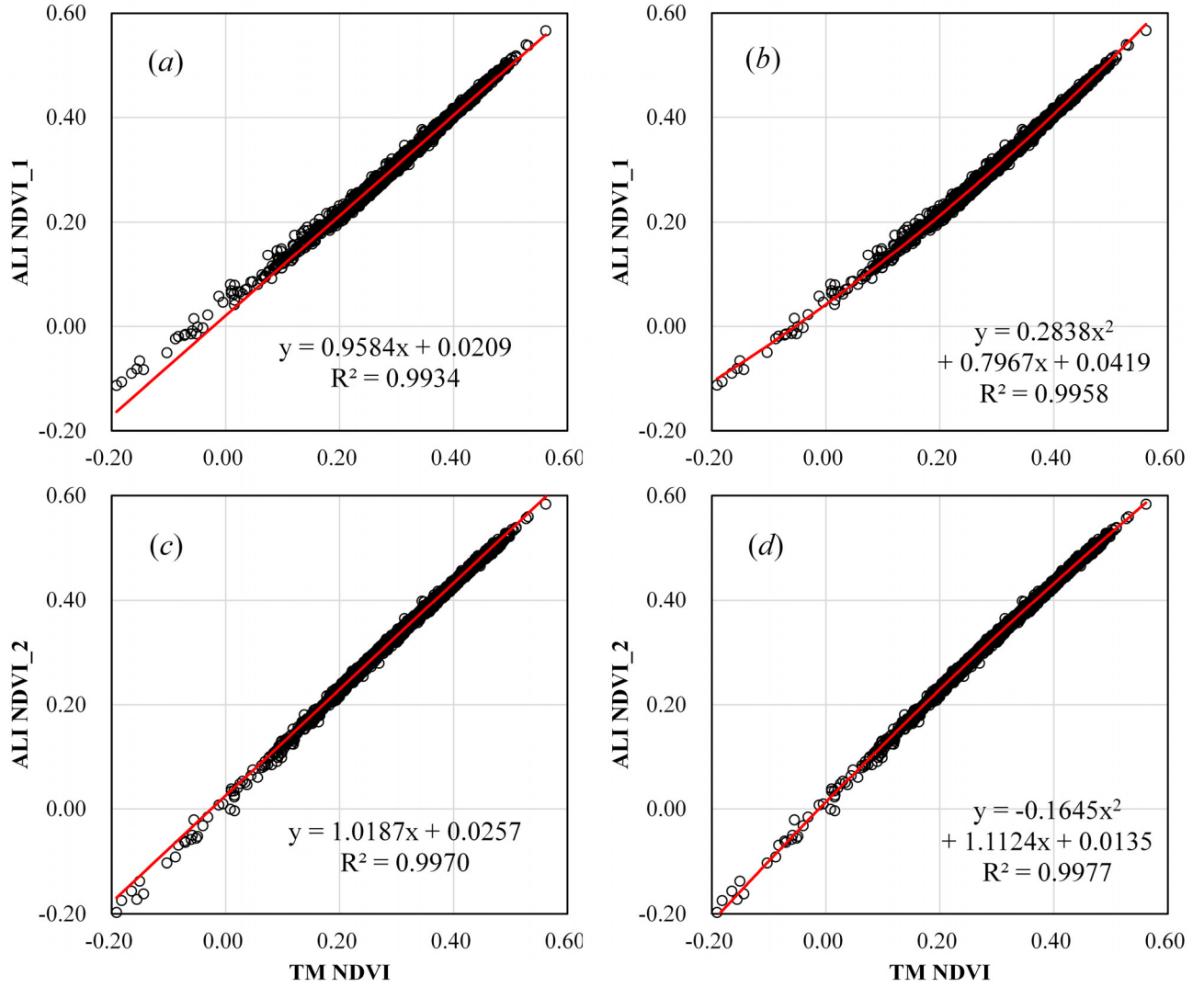


Fig. 4. Performances of (a) and (c) generalized model and (b) and (d) simplified model for NDVI intercalibration.

TABLE II  
VALUES FOR MONTE CARLO SIMULATIONS

Factor	Values				
	TOC (cm <sup>2</sup> ·atm <sup>-1</sup> )	TPW (g·cm <sup>-2</sup> )	AOT	SBAF Red NIR	SZA (°)
TOC	0.25-0.48	1.0	0.5	1.0 1.0	30
TPW	0.37	0.0-2.0	0.5	1.0 1.0	30
AOT	0.37	1.0	0.0-1.0	1.0 1.0	30
SBAF	0.37	1.0	0.5	0.9-1.1 0.9-1.1	30
SZA	0.37	1.0	0.5	1.0 1.0	0-60

The simulated NDVI<sub>2</sub> values were plotted against the NDVI<sub>1</sub> values. If the scatterplot exhibited significant (insignificant) scattering, the candidate factor was considered critical (unimportant) for linear NDVI intercalibration. For those critical factors, linear regressions may yield less-than-unity  $R^2$  values and nonunit slope values. The factor may be more critical if the  $R^2$  and slope values deviate more from unity. Furthermore, if the scattering cannot be fitted with a quadratic function, the factor is also critical for quadratic

NDVI intercalibration. For the sake of conciseness, only ALI NDVI<sub>1</sub> was simulated.

#### IV. RESULT

##### A. Results of the Generalized and Simplified NDVI Intercalibrations

The performances of the generalized and simplified models are shown in Fig. 4. The x-axis denotes the intercalibrated TM NDVI and the y-axis denotes the ALI NDVI. For ALI NDVI<sub>1</sub>, the generalized model yields  $y = 1.0148x - 0.0112$  ( $R^2 = 0.9978$ ,  $A = 0.0063$ ,  $P = 0.0037$ , and  $U = 0.0074$ ) and the simplified model yields  $y = 0.9813x + 0.0120$  ( $R^2 = 0.9974$ ,  $A = -0.0061$ ,  $P = 0.0042$ , and  $U = 0.0074$ ). For ALI NDVI<sub>2</sub>, the generalized model yields  $y = 1.0200x - 0.0272$  ( $R^2 = 0.9984$ ,  $A = 0.0200$ ,  $P = 0.0037$ , and  $U = 0.0203$ ) and the simplified model yields  $y = 1.0129x - 0.0332$  ( $R^2 = 0.9982$ ,  $A = 0.0285$ ,  $P = 0.0036$ , and  $U = 0.0287$ ). Overall, the generalized model performs better than the simplified model. Comparatively, the accuracy values

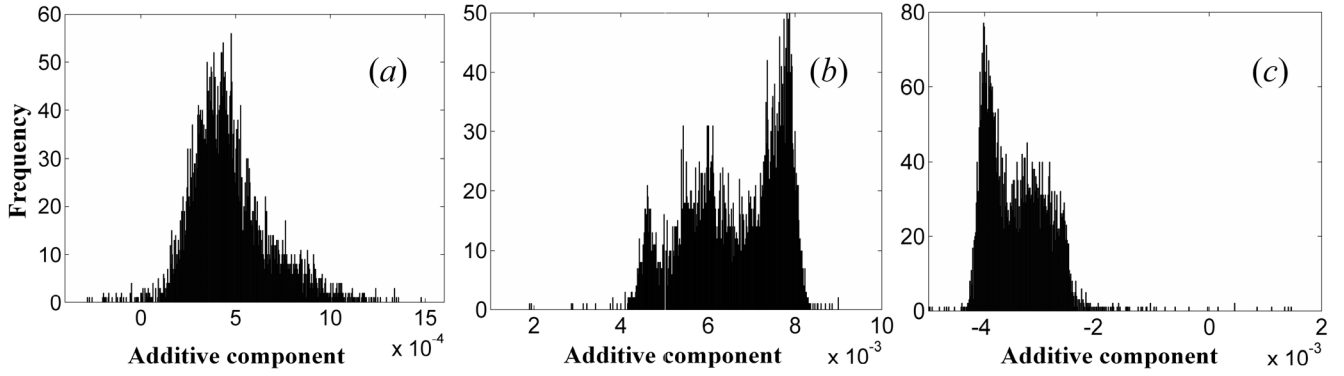


Fig. 5. Histograms of the additive components in (a) red band, (b) NIR<sub>1</sub> band, and (c) NIR<sub>2</sub> band.

are 0.0080/0.0315, the precision values are 0.0071/0.0047, and the uncertainty values are 0.0106/0.0318 for the unprocessed NDVIs. In terms of uncertainty values, the generalized model improves NDVI consistency by  $\sim 30\%/ \sim 36\%$  and the simplified model improves NDVI consistency by  $\sim 30\%/ \sim 10\%$ , respectively, for the two NDVIs.

To validate the assumption of  $b_R \ll 1$  and  $b_N \ll 1$  in the derivation of (4), Fig. 5 shows histograms of the additive components in the red and the NIR bands. The values of  $b_R$  are within  $-0.0003 \sim 0.0015$ , and the values of  $b_N$  are within  $0.0019 \sim 0.0090$  and  $-0.0050 \sim 0.0015$ , respectively, for the two infrared bands. Therefore, the additive components are well within  $-0.01 \sim 0.01$  and (4) holds.

### B. Results of Linear and Quadratic Intercalibrations

Linear and quadratic functions for NDVI intercalibration are shown in Fig. 6. The  $x$ -axis denotes TM NDVI, and the  $y$ -axis denotes ALI NDVI. For ALI NDVI<sub>1</sub>, the linear function is  $y = 0.9584x + 0.0209$  ( $R^2 = 0.9934$ ,  $A = 0.0000$ ,  $P = 0.0062$ , and  $U = 0.0062$ ). ALI NDVI<sub>1</sub> is generally higher than TM NDVI, especially for low NDVI values. The differences are well corrected by the quadratic function  $y = 0.2832x^2 + 0.7967x + 0.0419$  ( $R^2 = 0.9985$ ,  $A = 0.0000$ ,  $P = 0.0050$ , and  $U = 0.0050$ ). For ALI NDVI<sub>2</sub>, the linear function is  $y = 1.0187x + 0.0257$  ( $R^2 = 0.9970$ ,  $A = 0.0001$ ,  $P = 0.0044$ , and  $U = 0.0044$ ). ALI NDVI<sub>2</sub> is slightly higher than TM NDVI, especially for high NDVI values. Similar to ALI NDVI<sub>1</sub>, the quadratic function yields better NDVI consistency ( $y = -0.1645x^2 + 1.1124x + 0.0135$ ;  $R^2 = 0.9977$ ,  $A = 0.0000$ ,  $P = 0.0039$ , and  $U = 0.0039$ ).

### C. Major Factors of NDVI Intercalibration

The effects of TOC, TPW, AOT, SBAF, and SZA on NDVI intercalibration are shown in Fig. 7. Ozone generally has a minor effect on NDVI intercalibration when TOC varies between  $0.25 \sim 0.48 \text{ cm} \cdot \text{atm}^{-1}$ . The linear function is  $y = 1.0347x - 0.0408$  ( $R^2 = 0.9999$ ). Minor effects are also observed for aerosol ( $\text{AOT} = 0.0 \sim 1.0$ ) and SZA ( $\text{SZA} = 0 \sim 60^\circ$ ). The linear functions are  $y = 1.0349x - 0.0410$  ( $R^2 = 0.9999$ ) and  $y = 1.0356x - 0.0419$  ( $R^2 = 0.9999$ ). By contrast, water vapor has a significant effect on NDVI intercalibration when TPW ranges between  $0.0$  and  $2.0 \text{ g} \cdot \text{cm}^{-2}$ ,

especially for low NDVI values. The linear function is  $y = 1.0309x - 0.0362$  ( $R^2 = 0.9992$ ). However, it can be  $y = 0.985x + 0.015$ ,  $y = 1.064x - 0.064$ , or others in-between.

Spectral band differences have the most significant effects on NDVI intercalibration when SBAFs vary between  $0.9$  and  $1.1$ . The linear function is  $y = 1.0341x - 0.0406$  ( $R^2 = 0.9895$ ). However, it can be  $y = 0.920x + 0.080$ ,  $y = 1.205x - 0.205$ , or others in-between. Similar to water vapor, significant scattering patterns are also observed for low NDVI values. However, the scattering is less significant for high NDVI values. Overall, the  $R^2$  value is  $0.9895$  for SBAF, followed in an increasing order by  $0.9992$  for TPW and  $0.9999$  for other factors. Based on these results, spectral band difference is the most critical factor for NDVI intercalibration followed by water vapor.

## V. DISCUSSION

### A. Applicability of Linear Functions for NDVI Intercalibration

Fig. 7 shows the minor effects of TOC, AOT, and SZA on NDVI intercalibration. If a linear function has been developed over a specific area, it can be still applicable under varying TOC, AOT, and SZA conditions. Ozone and aerosol effects are band-dependent, and are similar for analogous bands of TM and ALI. However, the degree of water vapor effect is related to the ratio of atmospheric absorption transmittances. Based on this point, several findings can be noted. First, the variation in transmittance ratio is insignificant for low water vapor content. Therefore, linear functions can be transferable over arid land. Second, a linear function can be highly accurate in the case of a horizontally homogeneous atmosphere, where the ratio remains spatially invariant. Third, a linear function may cause large errors when sensors differ in the NIR bands. For instance, if one NIR band is affected by water vapor absorption and the other is unaffected. In this case, the linear function may yield a high  $R^2$  value; however, large uncertainties occur for low NDVI values.

Surface reflectance is probably the most critical factor for the use of a linear function. Based on the given RSRs, the SBAF is determined exclusively by surface reflectance. Therefore, the factor is likely to be land cover-dependent [45]. In Fig. 7(d), the SBAF has a significant effect on NDVI



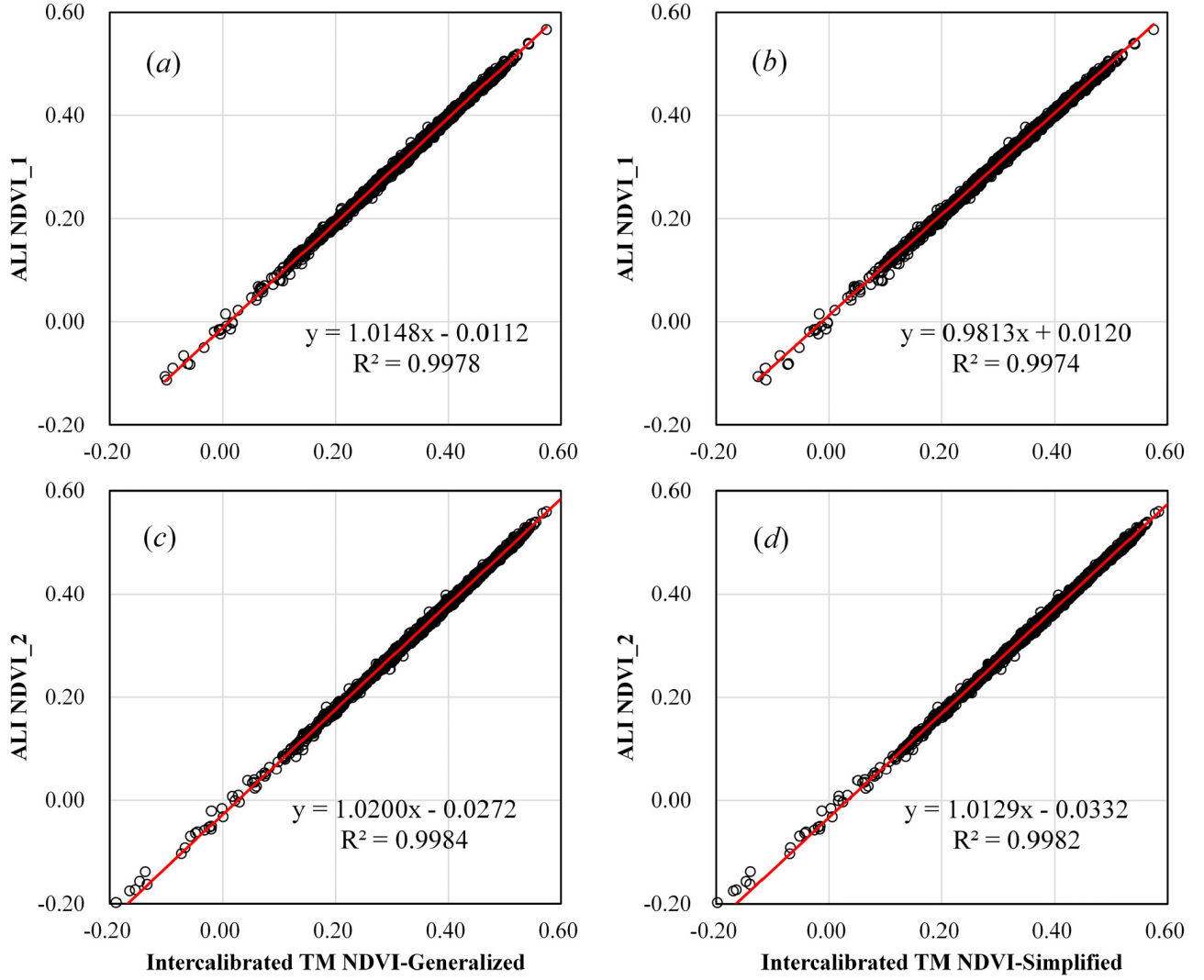


Fig. 6. Linear and quadratic functions for NDVI intercalibration. (a) and (b) Functions of TM NDVI and ALI NDVI<sub>1</sub>. (c) and (d) Functions of TM NDVI and ALI NDVI<sub>2</sub>.

intercalibration, especially for low NDVI values. Thus, linear functions may perform poorly over mixed land cover types, especially in areas with mosaics of water surfaces and/or bare lands, where NDVI is generally low. In contrast, linear functions are readily applicable over unique land cover types. This has been demonstrated in [29], in which linear functions are only applied to a rice canopy.

In fact, a simple mathematical treatment of (4) yields the following equation:

$$\text{NDVI}_2 = \underbrace{\frac{1}{1 + \varphi \times \text{NDVI}_1}}_{\text{multiplicative}} \text{NDVI}_1 + \underbrace{\frac{\varphi}{1 + \varphi \times \text{NDVI}_1}}_{\text{additive}} \quad (6)$$

where  $\varphi = n_2/n_1$ . In general, any factor can affect NDVI intercalibration by changing  $\varphi$ . This paper reveals that  $\varphi$  has a weak dependence on ozone concentration, AOT, and SZA, and a strong dependence on water vapor content and surface reflectance. In general, the use of linear functions is a compromise between different  $\varphi$  and NDVI<sub>1</sub> values. For identical

sensors,  $\varphi$  is equated to zero, and  $\text{NDVI}_2 = \text{NDVI}_1$ . The multiplicative component is an increasing function of NDVI when  $\varphi < 0$ , and the additive component is an unconditionally decreasing function of NDVI. Therefore, the multiplicative component (slope) may play an important role for high NDVI values, and the additive component (intercept) may play a more important role for low NDVI values. Therefore, Fig. 7(b) and (d) exhibit significant scattering for low NDVI values and insignificant scattering for high NDVI values.

#### B. Applicability of Quadratic Functions for NDVI Intercalibration

Quadratic functions are generally more accurate than linear functions for NDVI intercalibration (Section IV-B). However, it seems that the wedge-shaped pattern of NDVI differences in Fig. 7(d) cannot be corrected by either method. This issue can be explained by the dependencies of the red band SBAF and the NIR band SBAF. In Fig. 7(d), the SBAF varies between 0.9 and 1.1 independently for both bands.

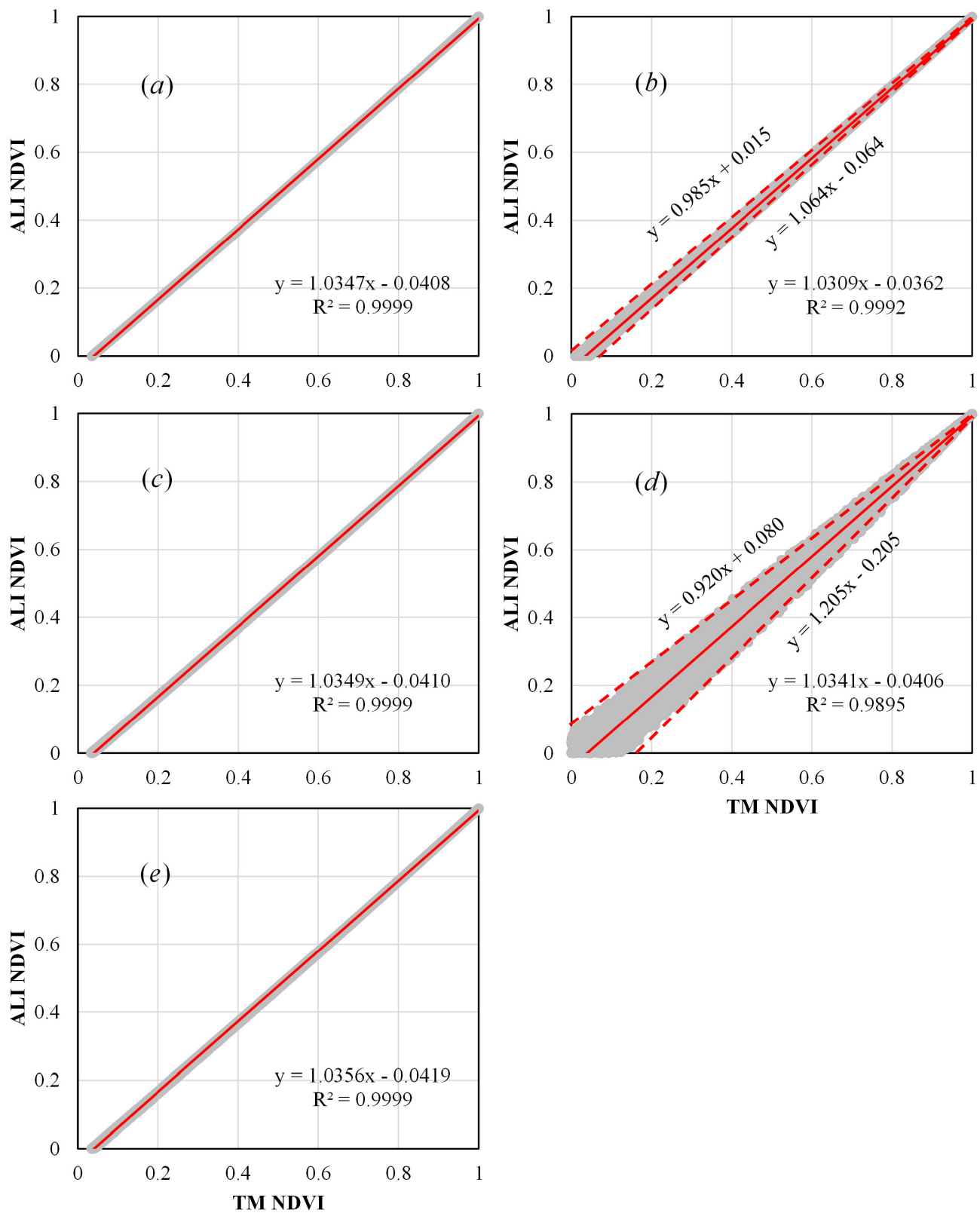


Fig. 7. Effects of (a) ozone, (b) water vapor, (c) aerosol, (d) spectral band difference, and (e) SZA on linear NDVI intercalibration.

However, their dependencies should be considered in simulations. Dual-band SBAFs are derived from the same Hyperion surface reflectances, and are therefore highly correlated.

In addition, NDVIs are also calculated from TOA reflectances. Thus, the SBAFs are strongly dependent on NDVI (Fig. 8). The dependencies may partly support the use of quadratic



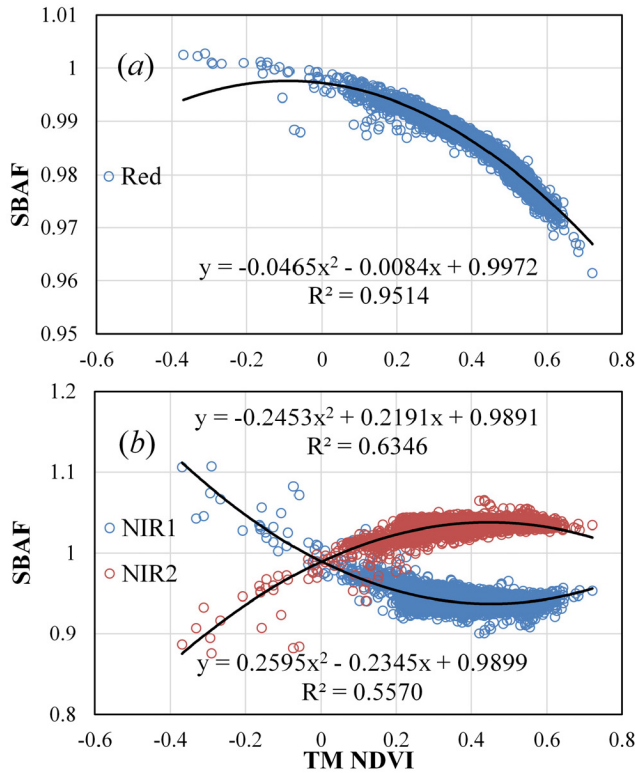


Fig. 8. Relationships between TM NDVI and SBAF in (a) red and (b) NIR bands.

functions for NDVI intercalibrations. However, a quadratic function is still not a cure-all solution to multisensor NDVI inconsistency problems. Although the wedge-shaped differences in Fig. 7(d) may be corrected, this is not the case for those in Fig. 7(b). If water vapor is unevenly distributed in space, quadratic functions still cannot fully address the NDVI differences.

In fact, the quadratic relationship between SBAF and NDVI holds, irrespective of surface reflectance. SBAFs are derived from surface reflectances, while NDVIs are calculated from TOA reflectances. The atmosphere may cause discrepancies between the two reflectance data sets. However, it is not the dominant factor, especially for a bright surface or a clear atmosphere. Therefore, the SBAFs are inherently dependent on NDVI. The strength of dependence is likely controlled by the degree of spectral overlap. According to the figure-of-merit index proposed in [46], the red bands are mostly overlapped, followed by the TM NIR/ALI NIR<sub>2</sub> bands and the TM NIR/ALI NIR<sub>1</sub> bands. Correspondingly, the  $R^2$  values are 0.9514, 0.6346, and 0.5570 between red band SBAF, NIR<sub>1</sub> band SBAF, NIR<sub>2</sub> band SBAF, and TM NDVI (Fig. 8), respectively. High  $R^2$  values indicate better band-to-band intercalibration, and thus better NDVI intercalibration. As a result, Fig. 6 shows better intercalibration results for TM NDVI/ALI NDVI<sub>2</sub> than TM NDVI/ALI NDVI<sub>1</sub>. Inferred from this point, NDVI intercalibration is more difficult if sensor bands are spectrally dissimilar.

The statistical dependencies between SBAFs and NDVI provide a novel idea to calculate SBAFs. In this paper, SBAFs are calculated by convolving Hyperion surface

reflectance data, which is impracticable over areas without hyperspectral images [47]. As shown in Fig. 8, it is likely that SBAFs can be estimated using simple spectral indices such as NDVI. Alternatively, continuous surface reflectances can be initially simulated from historical satellite data via interpolation methods (e.g., in [48]) and then calculated for SBAFs. Despite all that, these approximate methods need further examinations.

### C. Uncertainties in NDVI Intercalibrations

Uncertainties in NDVI intercalibrations should be clearly addressed. According to (3) and (4), NDVI intercalibration is affected by multiple factors including atmospheric conditions (TOC, TPW, and AOT), sensor differences (SBAF), data processing methods (NDVI<sub>1</sub> and NDVI<sub>2</sub>), and model types (generalized, simplified, linear, and quadratic methods). Initially, atmospheric conditions play minor roles, except for water vapor. Even if water vapor has an impact, it is still less influential than spectral band differences. Overall, these factors affect NDVI intercalibration by changing  $\varphi$  in (6). By contrast, data processing methods affect NDVI intercalibration by changing NDVI itself (NDVI<sub>1</sub> and NDVI<sub>2</sub>). As a common practice, spatial aggregation is used to reduce the effects of spatial misregistration and imaging differences [49]. Moreover, model-induced uncertainty should be evaluated. Most operational models are derived with assumptions. For instance, spherical atmospheric albedo is neglected in this paper to derive (3), and small values are neglected to derive (4). With our models, these uncertainties can be easily quantified.

Uncertainties may also result from different processing schemes. Most current studies transform spectral bands into NDVI and then perform NDVI intercalibrations. While this paper first performs spectral band intercalibrations and then transforms the intercalibrated bands into NDVI. Recent study indicates that the NDVI-to-NDVI scheme outperforms the band-to-band scheme [34]. It is likely that our model can provide insight into the inner differences.

## VI. CONCLUSION

This paper presents a generalized model and its simplified form for multisensor NDVI intercalibration. The simplified model provides a tool to evaluating current NDVI intercalibration methods. First, surface reflectance is the most critical factor for linear NDVI intercalibration followed by water vapor. The linear method may be problematic in areas with mixed land cover types or horizontally heterogeneous water vapor. It is generally less effective for low NDVI values, while other atmospheric parameters and SZA have minor impacts on the linear method. Second, there are inherently strong correlations between SBAFs and NDVI, which forms the basis of quadratic NDVI intercalibration. However, the quadratic method is still unable to treat the scenes with significant spatial variations in water vapor. Finally, the uncertainties associated with NDVI intercalibration are summarized as resulting from atmospheric condition, spectral band, data processing scheme, and model assumption differences.

Although our model in its present form is inadequate for operational use, it does provide backup information for evaluating current NDVI intercalibration methods. The results of this paper would deepen our understanding of multisensor NDVI intercalibration, and the proposed methods can be applied to other spectral indices. Future work needs to focus on the estimation of SBAFs in areas without hyperspectral images.

#### APPENDIX

The definition of SBAF is as follows:

$$f = \frac{\int_r \rho(\lambda) RSR(\lambda) d\lambda}{\int_s \rho(\lambda) RSR(\lambda) d\lambda} \quad (A1)$$

where  $\rho$  denotes surface reflectance at wavelength  $\lambda$ ,  $RSR$  denotes the RSRs of the reference sensor  $r$  and the subject sensor  $s$ .

In reflective solar bands,  $T_g$  can be approximated as follows:

$$T_g = T_{g,Ozone} * T_{g,Vapor} \quad (A2)$$

where  $T_{g,Ozone}$  and  $T_{g,Vapor}$  denote ozone transmittance and water vapor transmittance, each can be approximated as follows:

$$T_{g,Ozone} = \exp(a_0 * m * TOC) \quad (A3)$$

$$T_{g,Vapor} = \exp \left( - \exp \left( \frac{b_0 + b_1 * \ln(m * TPW)}{+ b_2 * \ln^2(m * TPW)} \right) \right) \quad (A4)$$

where  $m$  denotes air mass, and  $a_0$ ,  $b_0$ ,  $b_1$ , and  $b_2$  are sensor band-dependent coefficients.

$T_{s(v)}$  can be approximated as follows:

$$T_{s(v)} = c_0 + c_1 * m * AOT + c_2 * m / (1 + m) \quad (A5)$$

where  $c_0$ ,  $c_1$ , and  $c_2$  are sensor band-dependent coefficients.

$\rho_a$  can be approximated as follows:

$$\rho_a = d_0 + d_1 * AOT \quad (A6)$$

where  $d_0$  and  $d_1$  are sensor band-dependent coefficients.

#### ACKNOWLEDGMENT

The authors would like to thank anonymous reviewers for their constructive comments on an early version of this paper. Landsat-5 TM, EO-1 ALI, and Hyperion data sets were acquired from the Earth Resources Observation and Science Center, United States Geological Survey. TERRA MODIS data sets were acquired from LAADS Web Level 1 and the Atmosphere Archive and Distribution System, Goddard Space Flight Center.

#### REFERENCES

- [1] A. Anyamba and C. J. Tucker, "Analysis of Sahelian vegetation dynamics using NOAA-AVHRR NDVI data from 1981–2003," *J. Arid Environ.*, vol. 63, no. 3, pp. 596–614, Nov. 2015.
- [2] N. Pettorelli, J. O. Vik, A. Mysterud, J. M. Gaillard, C. J. Tucker, and N. C. Stenseth, "Using the satellite-derived NDVI to assess ecological responses to environmental change," *Trends Ecol. Evol.*, vol. 20, no. 9, pp. 503–510, Oct. 2005.
- [3] R. S. Defries and J. G. R. Townshend, "NDVI-derived land cover classifications at a global scale," *Int. J. Remote Sens.*, vol. 15, no. 17, pp. 3567–3586, Nov. 1994.
- [4] R. Fensholt, K. Rasmussen, T. T. Nielsen, and C. Mbow, "Evaluation of earth observation based long term vegetation trends—Intercomparing NDVI time series trend analysis consistency of Sahel from AVHRR GIMMS, Terra MODIS and SPOT VGT data," *Remote Sens. Environ.*, vol. 113, no. 9, pp. 1886–1898, Sep. 2009.
- [5] P. M. Teillet, J. I. Barker, B. I. Markham, R. R. Irish, G. Fedosejevs, and J. C. Storey, "Radiometric cross-calibration of the Landsat-7 ETM+ and Landsat-5 TM sensors based on tandem data sets," *Remote Sens. Environ.*, vol. 78, no. 1, pp. 39–54, Oct. 2001.
- [6] G. Chander *et al.*, "Applications of spectral band adjustment factors (SBAF) for cross-calibration," *IEEE Trans. Geosci. Remote Sens.*, vol. 51, no. 3, pp. 1267–1281, Mar. 2013.
- [7] G. Chander, B. L. Markham, and D. L. Helder, "Summary of current radiometric calibration coefficients for Landsat MSS, TM, ETM+, and EO-1 ALI sensors," *Remote Sens. Environ.*, vol. 113, no. 3, pp. 893–903, May 2009.
- [8] P. M. Teillet, G. Fedosejevs, K. J. Thome, and J. L. Barker, "Impacts of spectral band difference effects on radiometric cross-calibration between satellite sensors in the solar-reflective spectral domain," *Remote Sens. Environ.*, vol. 110, no. 3, pp. 393–409, Mar. 2007.
- [9] C. J. Tucker, "Red and photographic infrared linear combinations for monitoring vegetation," *Remote Sens. Environ.*, vol. 8, no. 2, pp. 127–150, Jun. 1979.
- [10] E. Vermote, N. El Saleous, Y. J. Kaufman, and E. Dutton, "Stratospheric aerosol perturbing effect on the remote sensing of vegetation: Correction method for the composite NDVI after the Pinatubo eruption," *Remote Sens. Rev.*, vol. 15, nos. 1–4, pp. 7–22, Feb. 1994.
- [11] J. C. N. Epiphanio and A. R. Huete, "Dependence of NDVI and SAVI on sun/sensor geometry and its effect on fAPAR relationships in Alfalfa," *Remote Sens. Environ.*, vol. 51, no. 3, pp. 351–360, Nov. 1994.
- [12] G. Guyot and X. F. Gu, "Effect of radiometric corrections on NDVI-determined from SPOT-HRV and Landsat-TM data," *Remote Sens. Environ.*, vol. 49, no. 3, pp. 169–180, Sep. 1994.
- [13] M. Roderick, R. Smith, and S. Cridland, "The precision of the NDVI derived from AVHRR observations," *Remote Sens. Environ.*, vol. 56, no. 1, pp. 57–65, Sep. 1995.
- [14] E. Tarnavsky, S. Garrigues, and M. E. Brown, "Multiscale geostatistical analysis of AVHRR, SPOT-VGT, and MODIS global NDVI products," *Remote Sens. Environ.*, vol. 112, no. 2, pp. 535–549, Feb. 2008.
- [15] M. D. Steven, T. J. Malthus, F. Baret, H. Xu, and M. J. Chopping, "Intercalibration of vegetation indices from different sensor systems," *Remote Sens. Environ.*, vol. 88, no. 4, pp. 412–422, Dec. 2003.
- [16] H. Yoshioka, T. Miura, and A. R. Huete, "An isoline-based translation technique of spectral vegetation index using EO-1 Hyperion data," *IEEE Trans. Geosci. Remote Sens.*, vol. 41, no. 6, pp. 1363–1372, Jun. 2003.
- [17] H. Yoshioka, H. Yamamoto, and T. Miura, "Analytical relationships of inter-sensor vegetation indices based on the theory of vegetation isoline," in *Proc. IGARSS*, vol. 6, Jul. 2005, pp. 4164–4167.
- [18] T. Miura, H. Yoshioka, and T. Suzuki, "Evaluation of spectral vegetation index translation equations for the development of long-term data records," in *Proc. IGARSS*, vol. 3, Jul. 2008, pp. III-712–III-715.
- [19] K. Taniguchi, K. Obata, and H. Yoshioka, "Investigation of inter-sensor NDVI relationships based on analytical representation of soil isolines," in *Proc. IGARSS*, Jul. 2012, pp. 4891–4894.
- [20] W. J. D. van Leeuwen, B. J. Orr, S. E. Marsh, and S. M. Herrmann, "Multi-sensor NDVI data continuity: Uncertainties and implications for vegetation monitoring applications," *Remote Sens. Environ.*, vol. 100, no. 1, pp. 67–81, Jan. 2006.
- [21] C. M. Beltran, A. Calera, and A. Jochum, "Intersatellite cross-calibration: Integration of reflectance and NDVI from different satellites by means of a linear model," *Proc. SPIE*, vol. 5232, pp. 128–139, Feb. 2004.
- [22] P. S. Thenkabail, "Inter-sensor relationships between IKONOS and Landsat-7 ETM+ NDVI data in three ecoregions of Africa," *Int. J. Remote Sens.*, vol. 25, no. 2, pp. 389–408, Jan. 2004.
- [23] C. Martínez-Beltrán, M. A. O. Jochum, A. Calera, and J. Meliá, "Multi-sensor comparison of NDVI for a semi-arid environment in Spain," *Int. J. Remote Sens.*, vol. 30, no. 5, pp. 1355–1384, Mar. 2009.
- [24] J. H. Anderson, K. T. Weber, B. Gokhale, and F. Chen, "Intercalibration and evaluation of ResourceSat-1 and Landsat-5 NDVI," *Can. J. Remote Sens.*, vol. 37, no. 2, pp. 213–219, Apr. 2011.
- [25] P. Li, L. Jiang, and Z. Feng, "Cross-comparison of vegetation indices derived from Landsat-7 enhanced thematic mapper plus (ETM+) and Landsat-8 operational land imager (OLI) sensors," *Remote Sens.*, vol. 6, no. 1, pp. 310–329, Dec. 2013.
- [26] T. Miura, H. Yoshioka, K. Fujiwara, and H. Yamamoto, "Inter-comparison of ASTER and MODIS surface reflectance and vegetation

- index products for synergistic applications to natural resource monitoring," *Sensors*, vol. 8, no. 4, pp. 2480–2499, Apr. 2008.
- [27] N. Rochdi and R. Fernandes, "Intercalibration of vegetation indices from Landsat ETM+ and MODIS 500m data for LAI mapping," Geomatics Canada, Chatham, U.K., Tech. Note 3, 2008.
- [28] Y. Kim, A. R. Huete, T. Miura, and Z. Jiang, "Spectral compatibility of vegetation indices across sensors: Band decomposition analysis with Hyperion data," *J. Appl. Remote Sens.*, vol. 4, no. 1, p. 043520, Mar. 2010.
- [29] W. Huang, J. Huang, X. Wang, F. Wang, and J. Shi, "Comparability of red/near-infrared reflectance and NDVI based on the spectral response function between MODIS and 30 other satellite sensors using rice canopy spectra," *Sensors*, vol. 13, no. 12, pp. 16023–16050, Dec. 2013.
- [30] A. Gonsamo and J. M. Chen, "Spectral response function comparability among 21 satellite sensors for vegetation monitoring," *IEEE Trans. Geosci. Remote Sens.*, vol. 51, no. 3, pp. 1319–1335, Mar. 2013.
- [31] J. Franke, V. Heinzl, and G. Menz, "Assessment of NDVI-differences caused by sensor-specific relative spectral response functions," in *Proc. IGARSS*, Jul./Aug. 2006, pp. 1138–1141.
- [32] A. P. Trishchenko, J. Cihlar, and Z. Q. Li, "Effects of spectral response function on surface reflectance and NDVI measured with moderate resolution satellite sensors," *Remote Sens. Environ.*, vol. 81, no. 1, pp. 1–18, Jul. 2002.
- [33] A. P. Trishchenko, "Effects of spectral response function on surface reflectance and NDVI measured with moderate resolution satellite sensors: Extension to AVHRR NOAA-17, 18 and METOP-A," *Remote Sens. Environ.*, vol. 113, no. 2, pp. 335–341, Feb. 2009.
- [34] P. D'Odorico, A. Gonsamo, A. Damm, and M. E. Schaepman, "Experimental evaluation of Sentinel-2 spectral response functions for NDVI time-series continuity," *IEEE Trans. Geosci. Remote Sens.*, vol. 51, no. 3, pp. 1336–1348, Mar. 2013.
- [35] M. A. Gilabert, S. Gandía, and J. Meliá, "Analyses of spectral-biophysical relationships for a corn canopy," *Remote Sens. Environ.*, vol. 55, no. 1, pp. 11–20, Jan. 1996.
- [36] Q. Wang, S. Adiku, J. Tenhunen, and A. Granier, "On the relationship of NDVI with leaf area index in a deciduous forest site," *Remote Sens. Environ.*, vol. 94, no. 2, pp. 244–255, Jan. 2005.
- [37] T. N. Carlson and D. A. Ripley, "On the relation between NDVI, fractional vegetation cover, and leaf area index," *Remote Sens. Environ.*, vol. 62, no. 3, pp. 241–252, Dec. 1997.
- [38] X. Fan and Y. Liu, "Quantifying the relationship between intersensor images in solar reflective bands: Implications for intercalibration," *IEEE Trans. Geosci. Remote Sens.*, vol. 52, no. 12, pp. 7727–7737, Dec. 2014.
- [39] X. Fan, Y. Liu, J. Tao, and Y. L. Weng, "Soil salinity retrieval from advanced multi-spectral sensor with partial least square regression," *Remote Sens.*, vol. 7, no. 1, pp. 488–511, Jan. 2015.
- [40] W. Chen, H. Zhao, Z. Li, X. Jing, and L. Yan, "Uncertainty evaluation of an in-flight absolute radiometric calibration using a statistical monte Carlo method," *IEEE Trans. Geosci. Remote Sens.*, vol. 53, no. 5, pp. 2925–2934, May 2015.
- [41] J. R. Nagol, E. F. Vermote, and S. D. Prince, "Effects of atmospheric variation on AVHRR NDVI data," *Remote Sens. Environ.*, vol. 113, no. 2, pp. 392–397, Feb. 2009.
- [42] D. R. Beck, "EO-1 user guide, version 2.3," Satellite Syst. Branch, USGS Earth Resour. Observ. Syst. Data Center, Sioux Falls, SD, USA, Tech. Rep., 2003.
- [43] T. Cooley *et al.*, "FLAASH, a MODTRAN4-based atmospheric correction algorithm, its application and validation," in *Proc. IGARSS*, vol. 3, Feb. 2002, pp. 1414–1418.
- [44] E. Vermote, D. Tanre, J. L. Deuze, and J. J. Morcette, "Second simulation of the satellite signal in the solar spectrum: An overview," *IEEE Trans. Geosci. Remote Sens.*, vol. 35, no. 3, pp. 675–686, May 1997.
- [45] X. Li *et al.*, "Radiometric cross-calibration of the CBERS-02 CCD camera with the TERRA MODIS," *Sci. China E, Eng. Mater. Sci.*, vol. 48, pp. 44–60, Dec. 2005.
- [46] G. Chander, A. Angal, T. Choi, D. J. Meyer, X. Xiong, and P. M. Teillet, "Cross-calibration of the Terra MODIS, Landsat 7 ETM+ and EO-1 ALI sensors using near-simultaneous surface observation over the Railroad Valley Playa, Nevada, test site," *Proc. SPIE*, vol. 6677, p. 66770Y, Oct. 2007.
- [47] B. R. Scarino *et al.*, "A Web-based tool for calculating spectral band difference adjustment factors derived from SCIAMACHY hyperspectral data," *IEEE Trans. Geosci. Remote Sens.*, vol. 54, no. 5, pp. 2529–2542, May 2016.
- [48] A. Röder, T. Kuemmerle, and J. Hill, "Extension of retrospective datasets using multiple sensors. An approach to radiometric intercalibration of Landsat TM and MSS data," *Remote Sens. Environ.*, vol. 95, no. 2, pp. 195–210, Mar. 2005.
- [49] D. G. Goodin and G. M. Henebry, "The effect of rescaling on fine spatial resolution NDVI data: A test using multi-resolution aircraft sensor data," *Int. J. Remote Sens.*, vol. 23, no. 18, pp. 3865–3871, Sep. 2002.



**Xingwang Fan** received the B.S. degree in surveying and mapping, and the M.S. degree in photogrammetry and remote sensing from Southeast University, Nanjing, China, in 2009 and 2012, respectively, and the Ph.D. degree in geographic information system from the Nanjing Institute of Geography and Limnology (NIGLAS), Chinese Academy of Sciences (CAS), Nanjing, in 2015.

He is currently an Assistant Professor with NIGLAS. His research interests include satellite data consistency and uncertainties in remote sensing.



**Yuanbo Liu** received the M.S. degree in physical geography from the Lanzhou Institute of Desert Research, Chinese Academy of Sciences (CAS), Nanjing, China, in 1994, and the Ph.D. degree in bioenvironmental sciences from Tottori University, Tottori, Japan, in 2003.

He is currently a Professor of Satellite Hydrology with the Nanjing Institute of Geography and Limnology, CAS. His research interests include quantitative remote sensing and hydrology.